LAWRENCE
LIVERMORE
NATIONAL
LABORATORY

UCRL-JRNL-213550

ELM Suppression in Low Edge Collisionality H-Mode Discharges Using n=3 Magnetic Perturbations

K. H. Burrell, T. E. Evans, E. J. Doyle, M. E. Fenstermacher, R. J. Groebner, A. W. Leonard, R. A. Moyer, T. H. Osborne, M. J. Schaffer, P. B. Snyder, P. R. Thomas, W. P. West, J. A. Boedo, A. M. Garofalo, P. Gohil, G. L. Jackson, R. J. La Haye, C. J. Lasnier, H. Reimerdes, T. L. Rhodes, J. T. Scoville, W. M. Solomon, D. M. Thomas, G. Wang, J. G. Watkins, L. Zeng

July 13, 2005

Plasma Physics and Controlled Fusion

ELM suppression in low edge collisionality H-mode discharges using n=3 magnetic perturbations

K.H. Burrell,[a] T.E. Evans,[a] E.J. Doyle,[b] M.E. Fenstermacher,[c] R.J. Groebner,[a] A.W. Leonard,[a] R.A. Moyer,[d] T.H. Osborne,[a] M.J. Schaffer,[a] P.B. Snyder,[a] P.R. Thomas,[e] W.P. West,[a] J.A. Boedo,[d] A.M. Garofalo,[f] P. Gohil,[a] G.L. Jackson,[a] R.J. La Haye,[a] C.J. Lasnier,[c] H. Reimerdes,[f] T.L. Rhodes,[b] J.T. Scoville,[a] W.M. Solomon,[g] D.M. Thomas,[a] G. Wang,[b] J.G. Watkins,[h] and L. Zeng[b]

[a] *General Atomics, P.O. Box 85608, San Diego, CA 92186-9784*

[b] *University of California, Los Angeles, California, USA*

[c] *Lawrence Livermore National Laboratory, Livermore, California, USA*

[d] *University of California, San Diego, California, USA*

[e] *CEA Cadarache EURATOM Association, Cadarache, France*

[f] *Columbia University, New York, New York, USA*

[g] *Princeton Plasma Physics Laboratory, Princeton, New Jersey, USA*

[h] *Sandia National Laboratories, Albuquerque, New Mexico, USA*

Abstract. Using resonant magnetic perturbations with toroidal mode number $n = 3$, we have produced H-mode discharges without edge localized modes (ELMs) which run with constant density and radiated power for periods up to about 2550 ms (17 energy confinement times). These ELM suppression results are achieved at pedestal collisionalities close to those desired for next step burning plasma experiments such as ITER and provide a means of eliminating the rapid erosion of divertor components in such machines which could be caused by giant ELMs. The ELM suppression is due to an enhancement in the edge particle transport which reduces the edge pressure gradient and pedestal current density below the threshold for peeling-ballooning modes. These $n = 3$ magnetic perturbations provide a means of active control of edge plasma transport.

1. INTRODUCTION

In order to have sufficient energy confinement to reach burning plasma conditions, next step devices such as ITER [1] will operate in H-mode. This choice, however, comes at a significant potential cost because of the effects of edge localized modes (ELMs), which typically occur in H-mode. Although ELM-induced particle transport has a beneficial effect in allowing density and impurity control, the pulsed heat load to the divertor plates at the anticipated pedestal collisionality $\nu_e^* \sim 0.1$ in ITER is large enough to cause rapid erosion of those plates [2-4]. As part of an international effort to develop controlled ELM regimes, we have recently produced co-injected, ELM-free H-mode plasmas which exhibit constant density and constant radiated power levels. This ELM suppressed state is made using resonant magnetic perturbations (RMPs) with toroidal mode number $n = 3$ created by the DIII-D I-coil. Although the use of magnetic perturbations is common to this mode of operation and previously reported ELM control results [5-10], the present results were achieved at much lower density, giving a pedestal collisionalities ($\nu_i^* \cong 0.02$ and $\nu_e^* \cong 0.2$ [11]) which are close to the anticipated ITER values.

As is shown in figure 1, we have produced H-mode plasmas which operate without ELMs for durations up to 2550 ms (about 17 energy confinement times); the duration is limited only by hardware constraints, not by plasma physics issues. The suppression of ELMs in these plasmas is due to enhanced edge particle transport caused by the RMPs, coupled with cryopumping, which allows us to reduce the pedestal densities and pressures so that the edge plasma becomes stable to the peeling-ballooning modes which drive the ELMs [12,13]. Peeling-ballooning mode stability analysis for these discharges demonstrates that the edge plasmas are in the stable region of parameter space. In spite of reducing the pedestal pressure, we have created ELM suppressed plasmas which exhibit only a minor, 10% reduction in the global energy confinement. More importantly, by altering the current in the I-coil and using gas puffing, we can actively control the edge

density and pressure to keep the plasma in the stable parameter regime for peeling-ballooning modes.

Although we have limited theoretical understanding of why the RMPs alter the particle transport, we have built up a significant body of empirical knowledge of how this tool works. First, the reduction of density with the RMPs demonstrates that the RMP-induced particle transport exceeds that produced by the ELMs themselves. This change in transport increases with increasing I-coil current. Second, the transport alteration is a resonant effect, seen to date in a narrow window in the edge safety factor q_{95} = 3.6±0.2, which brackets the 11/3 value of one of the dominant Fourier harmonics of the I-coil; this harmonic has poloidal mode number $m = 11$ and $n = 3$. Operationally, suppression of the ELMs requires the magnitude of this harmonic to be $\delta b_r^{(11,3)} / B_T \geq 1.4 \times 10^{-3}$; here B_T is the vacuum toroidal field at the plasma center. (This δb_r corresponds to a 2 kA current in the I-coil.) In addition, ELM suppression requires a neutral beam input power greater than about 4 MW and a pedestal density n_e^{ped} below about 2×10^{19} m^{-3} for the plasmas used to date.

There are significant differences between the present, low collisionality RMP results and the previous results on DIII-D at higher collisionality ($\nu_e^* \sim 1$) [7-10,14]. The previous results showed rapid changes in the ELM character, typically within one ELM cycle (about 15 ms). However, even in the best cases, some Type I ELMs remained and, more importantly, considerable oscillation was seen in the divertor D_α traces, suggesting the continuing presence of small, Type II ELMs [14]. Unlike the low ν^* case, there is little if any change in the edge density and pressure profiles in the high ν^* plasmas. These results suggest a direct interaction between the RMP and the peeling-ballooning modes [14]. In the present, low ν^* case, while an immediate effect on the ELMs is also present, the complete ELM suppression takes place 100 to 150 ms after the RMP is turned on in discharges where all the other conditions for suppression are satisfied. As is

shown in figure 1, we can achieve complete ELM suppression for extended periods of time. Once the ELMs are suppressed, the D_α traces are extremely quiet with no hint of remnant Type II ELMs. In addition, the ELMs remain suppressed in some shots 100 to 150 ms after the RMP has been turned off. This demonstrates that the ELM suppression in the low ν^* case is not due to a direct interaction of the RMP field with the peeling-ballooning modes.

There are significant similarities between the present RMP suppressed H-modes and quiescent H-mode (QH-mode) plasmas [15,16]. The divertor D_α signals are equally quiet and the operating pedestal densities can be quite similar for similar plasma shapes. Both the RMP ELM-suppressed H-modes and QH-mode exhibit enhanced particle transport although the causes are different. In the case of QH-mode, the enhanced transport is caused by an edge electromagnetic mode, the edge harmonic oscillation (EHO), while in the present case it is the RMP itself. Indeed, in the present case, there is no sign of any mode like the EHO on the Mirnov loops. Both the RMP ELM-suppressed plasmas and the QH-mode [15] reach a transport equilibrium in the edge parameters located in the stable region for peeling-ballooning modes. The operating point for both types of discharges is located near the peeling stability boundary. A major difference between the two ELM-free states is the value and profile of the edge radial electric field E_r. This field has a much deeper minimum and a much greater shear near the separatrix in the QH-mode plasmas. Possibly because of this difference, the pedestal pressure is higher in QH-mode plasmas with the same shape and input power as the RMP discharges.

2. BASIC CONFIGURATION

As is shown in figure 2(a), the present experiments were done in lower single null divertor plasmas with modest triangularity. This shape was chosen because it couples well to the lower divertor cryopump when the outer divertor strike point is positioned as is shown in figure 2(a); the cryopump provides the particle exhaust needed for density control.

The three dimensional geometry of the I-coil is shown in figure 2(b); this coil was originally installed on DIII-D for resistive wall mode control [17]. As indicated in figure 2(a), it is located inside the DIII-D vacuum vessel, just behind the surface of the carbon protection tiles. In order to minimize the effect of the I-coil-produced RMPs on the core plasma, the toroidally adjacent segments of the I-coil are driven with opposite current polarities, producing an $n = 3$ toroidal mode structure. Positive current is defined to be in the counter-clockwise direction as viewed inward toward the toroidal axis and the corresponding perturbation field (δb_r) points in the direction of positive major radius R. The up/down parity of the coil is dubbed "even" when the upper and lower coil segments have the same polarity at each toroidal angle ϕ and "odd" when these polarities are opposite. The toroidal phase angle of the I-coil perturbations is two-fold symmetric; we define a toroidal phase of 0 deg to be when the current in the upper 30 deg I-coil segment is positive.

Based on results of some preliminary, piggyback experiments, we chose the 60 deg, even parity I-coil configuration for this experiment. The vacuum magnetic field perturbations produced by the I-coil for plasmas in the present experiment are shown in figure 3. Notice that the $m = nq$ location in these plasmas tracks along the maximum in δb_r. An additional nonaxisymmetric coil set, the so-called C-coil [18], was used in these experiments to compensate for field errors due to manufacturing irregularities in the

DIII-D coil set [18]. The vacuum field perturbations from this are not included in figure 3. Although almost all the shots in the present experiment had the 60 deg toroidal phasing, the one shot with 0 deg phasing showed significantly worse ELM suppression. This suggests that, in spite of the C-coil, there are still some nonaxisymmetric field components present in DIII-D.

3. CHANGES IN EDGE PARAMETERS DURING ELM SUPPRESSION

The key to the ELM suppression in the present experiments is the reduction in pedestal density and pressure caused by the application of the RMPs in cryopumped plasmas. This reduction is illustrated in figure 4. As can be seen there, after the I-coil current is turned on to create the RMP, the pedestal density, pedestal electron and pedestal ion pressures all drop. The major part of the change in the pedestal pressures is due to the reduction in pedestal density. Both discharges shown in figure 4 have cryopumping; the results clearly indicate greater particle exhaust with the RMP. Since the ultimate density in the ELM suppressed shot with the RMPs is lower than in ELMing shot, this indicates that the cross field particle transport in the presence of the RMPs is larger than the particle transport averaged over ELMs.

The changes in the pedestal profiles produced by the RMPs are shown in figure 5 for four different levels of the I-coil current. The RMP produces a monotone decrease in the pedestal pressure with increasing I-coil current. However, the behavior of the electron temperature is not as simple. As the I-coil current increases from 0 kA to 3 kA, the maximum electron temperature gradient actually increases, only decreasing at the highest I-coil current of 4 kA. This seems quite paradoxical, since one would naively expect that a radial magnetic field perturbation, possibly leading to an ergodic field structure, would reduce the electron temperature and temperature gradient. This behavior of the electron temperature, along with the strong effect of the RMPs on particle transport, are two of of the greatest puzzles posed by our present experimental results.

There are significant changes in the edge toroidal rotation and the edge E_r when the I-coil is applied and the ELMs are suppressed; these are shown in figure 6. As can be seen in figure 6(a), the edge toroidal rotation of the carbon ions actually increases in the steep gradient region near the separatrix within 70–90 ms of the time when the I-coil

turns on while the rotation further into the plasma remains about the same. Over the next several hundred milliseconds, the whole rotation profile increases, even out into the scrape-off layer. Using the carbon measurements to compute E_r shows [figure 6(b)] that the minimum in the edge E_r well changes little when the I-coil first comes on but the well becomes narrower because the E_r at points away from the minimum becomes more positive. This leads to an increase in the shear in E_r. After several hundred milliseconds, the E_r overall has become more positive, although the change in the minimum value is the least and the increased shear is still present. These changes in E_r are qualitatively what one would expect from the changes in the edge profiles seen in figures 5 and 6(a).

The results in figures 4 and 5 clearly demonstrate that we can alter the pedestal pressure using RMPs. Since the pedestal values set the boundary conditions for core transport, one would expect that this change in pedestal pressure would lead to a reduction in global energy confinement. As is seen in figure 7, this reduction does indeed occur, reaching about 20% at the highest I-coil current of 4 kA. The most interesting part of this plot, however, is the 2 and 3 kA results which show that the change in the global energy confinement relative to the ITER 98(y2) H-mode scaling [19] is only about 10%. Since this comparison is done using thermal energy confinement time, the increase in fast ion pressure at low densities does not enter into the comparison. These discharges exhibit clear core transport barriers; apparently, that barrier becomes stronger once the density is reduced and the ELMs are suppressed. This increase in core confinement somewhat compensates for the reduction in pedestal pressure and results in the relatively small change in global confinement.

In discharges with pedestal densities well below 2×10^{19} m^{-3}, the ELMs remain suppressed for periods of 100 to 150 ms after the I-coil current is turned off (cf shots 122334 and 122336 after 3200 ms). During this period, the pedestal density and pressure

increase until the ELMs return. The absence of ELMs during this period with zero I-coil current demonstrates that the ELM suppression is not due to a direct interaction of the RMP fields with the peeling-ballooning modes in the plasma.

4. OPERATING SPACE FOR ELM SUPPRESSION

We have investigated the parameter space for ELM suppression by varying the plasma current, I-coil current, pedestal density and neutral beam input power.

As is suggested by the results in figure 3, we expect the ELM suppression to be a resonant effect and the experimental data are consistent with this expectation. In a series of shots taken for resistive wall mode studies in 2004, continuous current ramping was used. In these shots, some of which are discussed in [8], ELM suppression was seen over a narrow window in $q_{95} = 3.6 \pm 0.2$. Since these shots were run for other purposes, the precise boundary of this window may be uncertain by 0.1 owing to minor changes in pedestal density and input power. Experiments conducted this year show the same q_{95} sensitivity. When we flattopped the plasma current to give $q_{95} = 3.6$, we were able to achieve the long periods of ELM suppression shown in figure 1. Previous shots with continuous current ramping exhibited a return of ELMs.

Once q_{95} is in the proper range, we find that there is a minimum I-coil current needed for ELM suppression. This is demonstrated in figure 8, where we see that the ELMs are not completely suppressed at an I-coil current of 2 kA. The highest I-coil current gives the earliest ELM suppression, indicating that the dependence on I-coil current is not simply a threshold. This continuing dependence is due to the increase in RMP-induced particle transport with I-coil current.

ELM suppression has been achieved to date only for pedestal densities below about 2×10^{19} m^{-3}, which is equivalent to $n_e^{ped} / n_G = 0.16$, where n_G is the Greenwald density [20]. This is demonstrated in figure 9, where we have used continuous deuterium gas injection to vary the density.

As is illustrated in figure 10, there is a lower threshold in input power of about 4 MW where the ELMs begin to return. We have used input powers up to 10 MW to date with no sign of the ELMs returning. Problems with core beta limits for these low triangularity plasmas have limited our exploration of higher power levels.

5. COMPARISON WITH PREVIOUS HIGH ν^* RMP RESULTS ON DIII-D

There are several significant differences in ELM suppression between the present, low ν^* results and the previous RMP results at high ν^* ($\nu_e^* \sim 1$) [7-10,14]. In assessing these, one needs to be aware of the difference in I-coil configuration between the two data sets. Unlike the present RMP results with even parity, 60 deg phasing, almost all of the high ν^* results were done with 0 deg, odd parity. There is one shot with both parities at high ν^* which showed approximately the same level of ELM suppression with both parities. Based on this result, we believe that the difference between the present and previous results is primarily due to the difference in ν^*.

In the previous experiments, the I-coil affected the ELM behavior substantially but was unable to produce the complete ELM suppression illustrated in figure 1. The divertor D_α traces still showed a complex set of small, residual oscillations, which may be Type II ELMs [14]. In contrast, the D_α traces in the present experiment are quite quiet after the ELMs are suppressed.

The edge density and temperature profiles showed little change in the previous experiments when the I-coil was turned on. The edge rotation was, however, reduced significantly. This behavior is almost the mirror image of the present results, where the edge density and pressure are significantly reduced, as shown in figures 4 and 5, but the edge rotation actually increases, as is shown in figure 6.

At both high and low ν^*, there are immediate changes in the ELM character when the I-coil is turned on. These are illustrated for the present results in figure 4. At high ν^*, these immediate changes are the only ones seen. In the present, low ν^* work, it takes another 100 to 150 ms for the ELMs to be completely suppressed, possibly due to the time needed for the edge current to evolve after the edge pressures change. The time for the loop voltage to settle to a new equilibrium after the I-coil turns on is consistent with this idea. Osborne has speculated that the immediate change in the ELM character may be due to the direct interaction of the RMPs with the peeling-ballooning modes [14], perhaps by disrupting the phase coherence of multiple toroidal and poloidal modes

needed to create the explosively growing, nonlinear phase of the ELM [21]. As was discussed previously, the time behavior of the complete ELM suppression shows that this direct effect of the RMPs on the peeling-ballooning modes is not the cause of the complete suppression.

6. COMPARISON WITH QH-MODE DISCHARGES IN DIII-D

There are several significant similarities between the present shots with RMP-induced ELM suppression and the previously discovered QH-mode plasmas on DIII-D [15,16]. Although most of the QH-mode work has been done in plasmas with different shapes, we do have some QH-mode discharges in the shape shown in figure 2 [16]. A comparison of one of these QH-modes with one of the present shots is shown in figure 11. The most visually striking similarity is the very quiet signals seen on the divertor D_α detectors. For both these shots, the ultimate operating pedestal density is about the same. However, as can be seen in figure 11, the ELMs cease in the QH-mode at a pedestal density about 50% above that for the RMP shot. In higher triangularity shapes, the QH-mode plasmas have significantly higher pedestal density thresholds [16]; we have not yet used the RMPs in these shapes. As is also shown in figure 11, the QH-mode plasma has appreciably higher pedestal electron and ion pressures even though the global energy confinement normalized to the ITER 98(y2) scaling is about the same. This difference in pedestal pressure is seen even in the latter phase of the two shots when the input power is the same.

The need for density control is common both to the QH-mode and the present, RMP cases. Cryopumping provides the ultimate particle exhaust in both cases. However, the mechanism providing the enhanced cross field particle transport appears to be completely different. In the QH-mode, there is an edge electromagnetic oscillation, the edge harmonic oscillation (EHO), which produces the additional cross field particle transport [15,16]. As is illustrated in figure 4, the RMP itself provides the extra cross field transport in the present case. This difference in particle transport mechanisms almost certainly explains the different sensitivity to q_{95} in the two cases. QH-mode is seen over a continuous range of $3.7 \le q_{95} \le 5.8$ while the RMP-induced exhibits a resonant window in q_{95}. The q_{95} range for QH-mode simply represents the range explored to date.

Perhaps the most important similarity between the two ELM-free discharge types is operation at edge parameters which are stable to peeling-ballooning modes. This is

discussed more extensively in the next section. The key point here is that we have two different techniques to achieve a transport equilibrium for the edge plasma at a point where the edge pressure gradients and edge currents are below those which trigger the peeling-ballooning modes.

There is a major difference in the edge E_r between the two types of discharges. This is shown in figure 12. Although the E_r values in the near scrape off layer are similar, the minimum in the E_r well just inside the separatrix is much deeper in QH-mode, producing a much greater E_r shear just inside the separatrix. The higher edge pressure and the opposite sign of the toroidal rotation contribution to E_r for the QH-mode both contribute to this difference.

7. STABILITY TO PEELING-BALLOONING MODES

For the present RMP-induced ELM suppression shots, we have performed an extensive set of stability analyses [14], comparing the measured edge operating points to the stability predictions from the ELITE code [20-22]. In figure 13, we compare the operating points for one of the present RMP shots and one of the highest triangularity QH-mode shots [14] with the ELITE results. For the nominal operating points shown in figure 13(b), the measured pressure profiles were used in the ELITE analysis. In addition, plasma shape was determined using the EFIT [24] MHD equilibrium code. Furthermore, the edge current profile was determined by combining EFIT equilibrium analysis (for the perpendicular, equilibrium current) with the Ohmic, Pfirsch-Schlüter and bootstrap currents (for the parallel currents) using the ONETWO transport code [25].

The qualitative changes in the stability boundary expected with increasing plasma shaping are indicated schematically in figure 13(a). Figure 13(b) shows the same qualitative dependence of the results, with the more weakly shaped, RMP plasma operating at lower pedestal pressures and currents. In both cases, the plasmas operate near the peeling stability boundary. In order to explore the stability boundaries more extensively, a series of model equilibria were created starting from the nominal operating point and then artificially perturbing the edge current density and edge pressure gradient. The variously colored squares in figure 12(b) are the results of these calculations.

In figure 14, we have combined the results from a number of the RMP-induced ELM suppression shots run in the present set of experiments. As can be seen there, the shots where the ELMs are suppressed are basically at or below the stability boundary within the error bars while the shots with clear Type I ELMs are beyond the stability boundary. In the ELMing cases, we chose time intervals for the analysis from the last 30% of the ELM cycle. Figure 14 documents an extremely important result: We are able to actively control the pedestal pressure so that we can move the edge operating point up to a factor of two below the stability boundary. In addition, altering the pedestal pressure also alters the pedestal current density.

8. DISCUSSION

The results of the present work leave us with a number of puzzles. The most pressing of these is the need to understand the mechanism that allows the RMPs to affect the edge plasma transport. As has been discussed previously [26], simple ideas about the effect of ergodic magnetic fields on radial transport would lead one to predict that their biggest effect would be to enhance the electron heat loss. This is based on the rapid electron thermal conductivity parallel to field lines. Because of the need to maintain ambipolar transport, particle transport effects would be expected to be smaller than electron thermal transport effects. However, in the present experiment, we see just the opposite. The RMPs produce a strong effect on the particle transport and a surprisingly weak effect on the electron thermal transport. The increase in the edge electron temperature gradient shown in figure 5 over a significant range of I-coil currents is a very surprising result.

The increase in particle transport is a common feature that has been seen in a number of experiments that utilized externally imposed nonaxisymmetric fields [26]. In addition, as was first seen on TEXT [27], externally imposed fields can lead to both decreases and increases in electron temperature gradients. Accordingly, the puzzle posed by the present results is common to a number of experiments on both limiter and divertor tokamaks. Before we can extrapolate the present results to future devices, we really need to develop a fundamental understanding of the mechanisms that produce the results we observe.

A related puzzle is the lack of change in the minimum in the edge E_r well just after I-coil turn on seen in figure 6(b). If the RMPs were creating an ergodic region in which field lines crossed the separatrix and connected with the walls, one would expect that the enhanced electron loss would result in a more positive E_r in the plasma edge over the whole region where enhanced electron loss occurs. This is what happens at points away from the minimum in the E_r well; however, the minimum value appears to be more resistant to change. Since the minimum value of E_r does not change, one must conclude that any region of enhanced electron loss due to parallel flow along perturbed magnetic fields must exist only outside of the minimum in E_r.

The E_r changes may be a key part of the physics which allows the increase in the edge electron and ion temperature gradients seen in figure 5. The shear in the edge E_r is known to play an important role in the creation of the H-mode edge transport barrier. The results in figure 6 show that the E_r shear increases after the I-coil is turned on. This increase may account for the increase in the edge electron and ion temperature gradients.

Another puzzle involves determining the exact magnetic field structure resulting from the combination of the externally imposed fields and the plasma response. Although we can do the vacuum field calculations as shown in figure 3, we do not have a complete understanding of how the plasma responds and shields out a portion of these fields [28-30]. This shielding may well be a key part of determining the effect on transport. An answer to this part of the question also bears on the sensitivity of the present results to the toroidal phasing of the RMP. Without an understanding of the plasma screening, we cannot calculate in detail the effect of the error fields (with or without the C-coil in operation); these may well have significant components which combine differently with the I-coil-produced RMP depending on the toroidal phase selected.

Although the poloidal mode spectrum of the I-coil is very different for even and odd parity, the sparse data that we have at high ν^* shows little difference between even and odd parity. Since both the low and high ν^* data experimentally show a resonant effect as q_{95} varies, it is quite puzzling that the two different poloidal mode number spectra give about the same result.

Finally, the present data and the QH-mode data both suggest that we have achieved ELM-free operation by increasing the edge transport sufficiently that pedestal pressure gradient and current density are reduced below the edge peeling-ballooning stability limit. A key question is whether there are any other transport control techniques which could be used to achieve the same result.

9. CONCLUSIONS

Using RMPs produced by the DIII-D I-coil, we have achieved H-mode plasmas with no ELMs which exhibit constant density and radiated power for long periods of time (2550 ms or about 17 energy confinement times). The duration of the ELM suppressed states is limited only by hardware constraints. These shots operate at pedestal collisionalities comparable to those needed for ITER. Comparisons with peeling-ballooning mode stability theory indicate that the ELMs are suppressed because the RMP-induced increase in edge transport reduces the edge pressure gradient and pedestal current density below the stability boundary. By varying the I-coil current and gas puffing, ELM suppressed discharges with only a 10% reduction in global energy confinement time can be reliably and reproducibly produced.

The long durations of ELM suppression were facilitated by lowering the pedestal density to $2.0 \times 10^{19}\ \mathrm{m}^{-3}$ and halting the plasma current ramp when q_{95} reached 3.6, the resonant value for the I-coil geometry. The $n = 3$ perturbation is necessary for producing the ELM-free state; identical discharges without the magnetic perturbation continued ELMing. The ELM-free state lasts for 100 to 150 ms after the I-coil current is gone, indicating that ELM suppression is due to changes in the edge plasma, not direct interaction with the peeling-ballooning modes.

These shots exhibit clear H-mode edge pedestals and H-mode levels of confinement ($H_{ITER98y2} \sim 1$). Parameter scans indicate a power threshold of about 4 MW and an I-coil current threshold of about 2 kA ($\delta b_r / B_T = 1.4 \times 10^{-3}$). To date, we have successfully created the ELM suppressed state at powers up to 10 MW and I-coil currents up to 4 kA with no sign of upper power or current limits. The $n = 3$ perturbation enhances the edge particle transport; this transport enhancement increases with I-coil current.

The results presented here demonstrate that the $n = 3$ RMPs provide us with a tool to actively control edge plasma transport in H-mode plasmas. By varying the I-coil current

and gas puff, we can continuously adjust the edge profiles as long as q_{95} is within the resonant window.

These ELM suppression results, in low collisionality plasmas, combined with previous results in DIII-D plasmas using the ITER scenario 2 shape at higher collisionality, significantly strengthen the physics basis for ELM suppression using $n = 3$ magnetic perturbations with a relatively simple coil set.

ACKNOWLEDGMENTS

This work was supported by the U.S. Department of Energy under DE-FC02-04ER54698, DE-FG03-01ER54615, W-7405-ENG-48(with UC,LLNL), DE-FG02-04ER54758, DE-FG02-89ER53297, DE-AC02-76CH03073, and DE-AC04-94AL85000.

REFERENCES

[1] ITER Physics Basis Document, Nucl. Fusion **39**, 2137 (1999).

[2] A.W. Leonard, R.J. Groebner, M.A. Mahdavi, T.H. Osborne, M.E. Fenstermacher, C.J. Lasnier, T.W. Petrie, Plasma Phys. Control Fusion **44**, 945 (2002).

[3] M.E. Fenstermacher, A.W. Leonard, P.B. Snyder, J.A. Boedo, N.H. Brooks, R.J. Colchin, D.S. Gray, R.J. Groebner, M. Groth, E. Hollman, C.J. Lasnier, T.H. Osborne, T.W. Petrie, D.L. Rudakov, H. Takahashi, J.G. Watkins, L. Zeng, Plasma Phys. Control Fusion **45**, 1597 (2003).

[4] A. Loarte, G. Saibene, R. Sartori, M. Becolet, L. Horton, T. Eich, A. Herrmann, M. Laux, G. Matthews, S. Jachmich, N. Asakura, A. Chankin, A. Leonard, G. Porter, G. Federici, M. Shimada, M. Sugihara, G. Janeschitz, J. Nucl. Mater. **313-316**, 962 (2003).

[5] H. Tamai, T. Shoji, K. Nagashima, Y. Miura, T. Yamauchi, H. Ogawa, H. Kawashima, T. Matsuda, M. Mori, K. Ida and S. Odachi, J. Nucl. Mater. **220-222**, 365 (1994).

[6] S.J. Fielding, R.J. Buttery, A.R. Field, P.B. Jones, H. Meyer, M. Valovic, H.R. Wilson, Proc. of 28th EPS Conf. on Controlled Fusion and Plasma Physics, Maderia, Portugal, 2001, Vol. 25A (European Physical Society, 2002) p. 1825.

[7] T.E. Evans, R.A. Moyer, P.R. Thomas, J.G. Watkins, T.H. Osborne, J.A. Boedo, E.J. Doyle, M.E. Fenstermacher, K.H. Finken, R.J. Groebner, M. Groth, J.H. Harris, R.J. La Haye, C.J. Lasnier, S. Mazusaki, N. Ohyabu, D.G. Pretty, T.L. Rhodes,

H. Reimerdes, D.L. Rudakov, M.J. Schaffer, G. Wang, L. Zeng, Phys. Rev. Lett. **92**, 235003-1 (2004).

[8] T.E. Evans, R.A. Moyer, J.G. Watkins, T.H. Osborne, P.R. Thomas, M. Becoulet, J.A. Boedo, M.E. Fenstermacher, K.H. Finken, R.J. Groebner, M. Groth, J.H. Harris, G.L. Jackson, R.J. LaHaye, C.J. Lasnier, S. Masuzaki, N. Ohyabu, D.G. Pretty, H. Reimerdes, T.L. Rhodes, D.L. Rudakov, M.J. Schaffer, M.R. Wade, G. Wang, W.P. West, and L. Zeng, Nucl. Fusion **45**, 595 (2005).

[9] T.E. Evans, R.A. Moyer, J.G. Watkins, P.R. Thomas, T.H. Osborne, J.A. Boedo, M.E. Fenstermacher, K.H. Finken, R.J. Groebner, M. Groth, J. Harris, G.L. Jackson, R.J. La Haye, C.J. Lasnier, and M.J. Schaffer, J. Nucl. Mater. **337-339**, (2005) 691.

[10] R.A. Moyer, T.E. Evans, T.H. Osborne, P.R. Thomas, M. Becoulet, J. Harris, K.-H. Finken, J.A. Boedo, E.J. Doyle, M.E. Fenstermacher, P. Gohil, R.J. Groebner, M. Groth, G.L. Jackson, R.J. LaHaye, C.J. Lasnier, A.W. Leonard, G.R. McKee, H. Reimerdes, T.L. Rhodes, D.L. Rudakov, M.J. Schaffer, P.B. Snyder, M.R. Wade, G. Wang, J.G. Watkins, W.P. West and L. Zeng, Phys. Plasmas **12**, 056119 (2005).

[11] O. Sauter, C. Angioni, Y.R. Lin-Liu, Phys. Plasmas **6**, 2834 (1999). Equations (18b) and (18c). For a multi-ion species plasma, we take $n_e Z$ in Eq. (18b) to be $n_e Z_{eff}$ while in Eq. (18c), we choose the deuteron collisionality and replace $n_i Z^4$

with $n_e Z_{eff}$ since $Z = 1$ for deuterons and the disparate species collisionality actually replaces $n_i Z^4$ with $n_i Z_i^2 Z_j^2$.

[12] P.B. Snyder, H.R. Wilson, J.R. Ferron, L.L. Lao, A.W. Leonard, T.H. Osborne, A.D. Turnbull, D. Mossessian, M. Murakami, X.Q. Xu, Phys. Plasmas **9**, 2037 (2002).

[13] P.B. Snyder, H.R. Wilson, J.R. Ferron, L.L. Lao, A.W. Leonard, D. Mossessian, M. Murakami, T.H. Osborne, A.D. Turnbull and X.Q. Xu, Nucl. Fusion **44**, 320 (2004).

[14] T.H. Osborne, P.B. Snyder, T.E. Evans, R.A. Moyer, M.J. Schaffer, K.H. Burrell, R.J. Groebner, A.W. Leonard, D.M. Thomas, G. Wang, L. Zeng, "Edge Stability Analysis and Pedestal and ELM Characteristics in I-Coil ELM Suppressed Discharges on D III-D, " in Proc. of 32nd EPS Conf. on Controlled Fusion and Plasma Physics, Tarragona, Spain 2005, (European Physical Society, 2005) (to be published).

[15] K.H. Burrell, M.E. Austin, D.P. Brennan, J.C. DeBoo, E.J. Doyle, C. Fenzi, C. Fuchs, P. Gohil, C.M. Greenfield, R.J. Groebner, L.L. Lao, T.C. Luce, M.A. Makowski, G.R. McKee, R.A. Moyer, C.C. Petty, M. Porkolab, C.L. Rettig, T.L. Rhodes, J.C. Rost, B.W. Stallard, E.J. Strait, E.J. Synakowski, M.R. Wade, J.G. Watkins, and W.P. West, Phys. Plasmas **8**, 2153 (2001).

[16] K.H. Burrell, W.P. West, E.J. Doyle, M.E. Austin, T.A. Casper, P. Gohil, C.M. Greenfield, R.J. Groebner, A.W. Hyatt, R.J. Jayakumar, D.H. Kaplan, L.L. Lao,

A.W. Leonard, M.A. Makowski, G.R. McKee, T.H. Osborne, P.B. Snyder, W.M. Solomon, D.M. Thomas, T.L. Rhodes, E.J. Strait, M.R. Wade, G. Wang, L. Zeng, Phys. Plasmas **12**, 056121 (2005).

[17] G.L. Jackson, et al., in Proc. of 30th EPS Conf. on Controlled Fusion and Plasma Physics, St. Petersburg, Russia (2003) P-4.47 on CDROM.

[18] J.T. Scoville and R.J. La Haye, Nucl. Fusion **43**, 250 (2003).

[19] ITER Physics Experts Groups, Nucl. Fusion **39**, 2208 (1999).

[20] M. Greenwald, J.L. Terry, S.M. Wolfe, S. Ejima, M.G. Bell, S.M. Kaye, G.H. Neilson, Nucl. Fusion **28**, 2199 (1988).

[21] P.B. Snyder, H.R. Wilson, X.Q. Xu, Phys. Plasmas **12**, 056115 (2005).

[22] P.B. Snyder, H.R. Wilson, J.R. Ferron, L.L. Lao, A.W. Leonard, T.H. Osborne, A.D. Turnbull, D. Mossessian, M. Murakami, X.Q. Xu, Phys. Plasmas **9**, 2037 (2002).

[23] P.B. Snyder, H.R. Wilson, J.R. Ferron, L.L. Lao, A.W. Leonard, D. Mossessian, M. Murakami, T.H. Osborne, A.D. Turnbull and X.Q. Xu, Nucl. Fusion **44**, 320 (2004).

[24] L.L. Lao, J.R. Ferron, R.J. Groebner, W. Howl, H. St. John, E.J. Strait, T.S. Taylor, Nucl. Fusion **30**, 1035 (1990).

[25] H.E. St John, J.R. Ferron, L.L. Lao, T.H. Osborne, S.J. Thompson, D. Wroblewski, Plasma Physics and Controlled Nuclear Fusion Research 1995 (Proc. 15th Int. Conf. Seville, 1994, International Atomic Energy Agency, Vienna, 1995), Vol. 3, 603.

[26] Ph. Ghendrih, A. Grossman, and H. Caps, Plasma Phys. Control Fusion **38**, 1653 (1996).

[27] T.E. Evans, J.S. deGrassie, G.L. Jackson, N. Ohyabu, A.J. Wootton, K.W. Gentle, W.L. Hodge, S.C. McCool, P.E. Phillips, T.L. Rhodes, R. Richards, Ch.P. Ritz, W.L. Rowan, F. Karger and G. Haas, J. Nucl. Mater. **145-146**, 812 (1987).

[28] T.H. Jensen, A.W. Leonard and A.W. Hyatt, Phys. Fluids B **5**, 1239 (1993).

[29] A.H. Boozer, Phys. Plasmas **3**, 4620 (1996).

[30] R. Fitzpatrick, Phys. Plasmas **5**, 3325 (1998).

FIGURE CAPTIONS

Fig. 1. Time history of tokamak discharge with the longest RMP-induced ELM suppression seen to date. (a) Plasma current and divertor D_α emission, showing complete absence of ELMs after 2440 ms, (b) pedestal ion and electron temperature, (c) line averaged density and pedestal density, (d) neutral beam input power and total power radiated from inside the separatrix, (e) ratio of thermal energy confinement time to the ITER 98(y2) H-mode scaling value showing these plasmas have H-mode levels of confinement, (f) I-coil current and q_{95} showing that q_{95} reaches the value needed for ELM suppression about 1600 ms, somewhat after the I-coil turns on at 1500 ms, (g) electron collisionality. These discharges are operated with feedback control of the neutral beam power to maintain constant stored energy; accordingly, P_{inj} is averaged over 50 ms to smooth the oscillations caused by the feedback.

Fig. 2. (a) Cross section of DIII-D showing the shape of the plasma used in the present experiments. Lower triangularity of this plasma is 0.36 while the upper triangularity is 0.19. Also shown on this cross section are the location of the cryopump entrance and the positions of the upper and lower portion of the I-coil. (b) The shape of the I-coil showing the direction of the perturbed radial magnetic field due to one of the segments. Segment current directions indicated are chosen for the even parity case.

Fig. 3. Color contour plot of the perturbed magnetic field of due to the I-coil as a function of poloidal mode number (abscissa) and radial position into the plasma (ordinate) for the shot shown in figure 4 at 4000 ms. Note the resonance line m=nq lies along a maximum of the perturbed field.

Fig. 4. Time history of two shots, one with I-coil-produced RMPs and one without. (a) Pedestal density, (b) pedestal electron pressure, (c) pedestal ion pressure, (d) divertor D_α signal showing ELMs, (e) energy confinement time normalized by plasma current to correct for minor 10% differences in plasma current time history, (f) I-coil current waveform. Note that the pedestal density, electron and ion pressure all fall when the I-coil turns on at 2000 ms in shot 122481. q_{95} is within the resonant window for the I-coil by the time the I-coil turns on at 2000 ms. Neither shot has deuterium gas injection during the time shown.

Fig. 5. Edge profiles of (a) total pressure, (b) electron density, (c) electron temperature and (d) ion temperature for different I-coil current levels. The case with no I-coil current is from a time just before an ELM. I-coil current levels are 0 kA (black), 2 kA (red), 3 kA (green), and 4 kA (blue).

Fig. 6. Radial profiles of (a) C VI toroidal rotation speed and (b) radial electric field for shot 122481 (see figure 4) at three times. The I-coil turns on at 2000 ms.

Fig. 7. Plot of pedestal pressure and thermal energy confinement time normalized to the ITER 98(y2) H-mode scaling as a function of current in the I-coil. For the shot with zero I-coil current, we show both the peak pedestal pressure and the pressure averaged over the ELM cycle.

Fig. 8. Time history of three shots with different I-coil current showing the effect of different current levels on the divertor D_α traces, indicating the changes in ELM behavior caused by the different I-coil currents.

Fig. 9. Time history of three shots with different gas injection rates resulting in different pedestal densities. The changes in the ELM behavior are shown by the three divertor D_α traces. I-coil current is 3.2 kA for these cases.

Fig. 10. Time history of three shots with different neutral beam input power resulting in different normalized beta levels. The changes in the ELM behavior are shown by the three divertor D_α traces. I-coil current is 3.0 kA for these cases.

Fig. 11. Time history of a counter-injected QH-mode shot (118720) and a co-injected shot (122342) with RMP-induced ELM suppression. (a) Pedestal electron density, (b) pedestal electron pressure, (c) pedestal ion pressure, (d) divertor D_α showing the difference in ELM behavior, (e) thermal energy confinement time normalized to the ITER 98(y2) scaling, (f) I-coil current, (g) neutral input power. Note that the pedestal pressures are higher for QH-mode even though the energy confinement times are quite similar.

Fig. 12. Comparison of the radial electric field near the separatrix for the two shots shown in figure 12. Analysis time is chosen so that the input power is similar. Note that the QH-mode E_r is much more negative inside the separatrix and, accordingly, has much greater shear near the separatrix.

Fig. 13. (a) Schematic illustration of the change in the peeling-ballooning mode stability boundary with plasma shape. Weak shaping is low triangularity while strong shaping is higher triangularity. (b) Plot of the stability results for a RMP plasma (shot 122342 at 4650 ms) and a QH-mode plasma (shot 115099 at 3500 ms). The actual operating points are shown by an X. The boxes are produced from using perturbations of the actual equilibria with different pressure gradients and edge current densities to map out the stability boundaries. Blue and green colors denote stability; red and orange denote instability. The x-axis is normalized maximum edge pressure gradient while the y-axis is the pedestal current density normalized to the average current density in the plasma.

Fig. 14. Peeling-ballooning mode stability diagram for a whole group of ELMing and RMP-induced ELM suppressed shots. As is indicated in the figure, the stability boundary is in the range of 0.5 to 2 for the normalized growth rate. The x-axis is normalized maximum edge pressure gradient while the y-axis is the pedestal current density normalized to the average current density in the plasma. Error in the determination of the location of a given point in this space is shown for one data point. Within this error bar, all the ELM suppressed shots are at the boundary of or within the stable region while the ELMing shots are at the boundary or beyond the stable region.

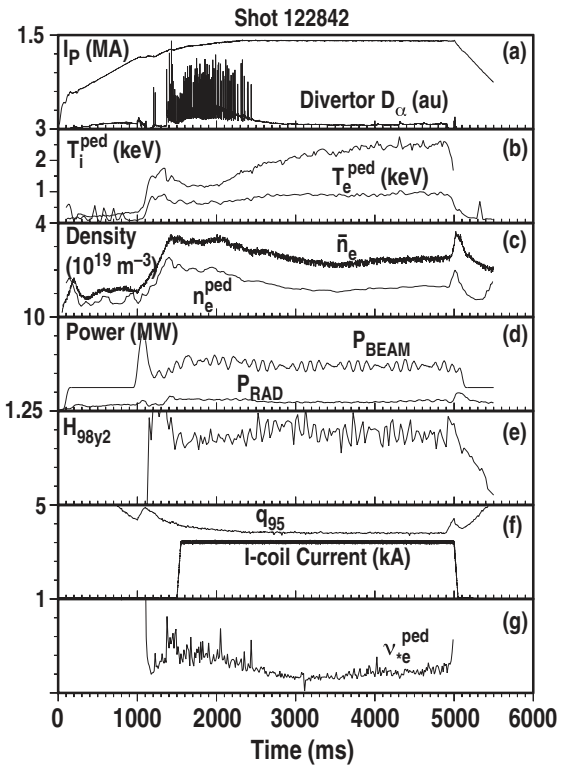

K.H. Burrell Figure 1

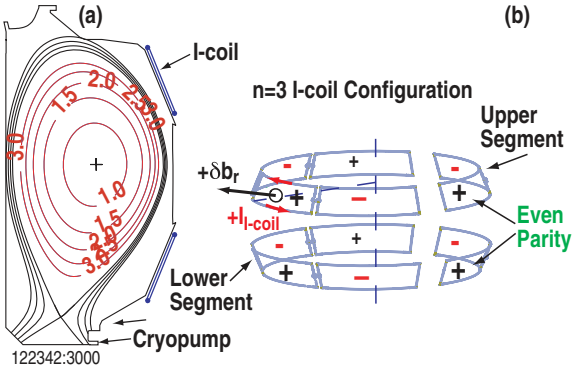

K.H. Burrell Figure 2

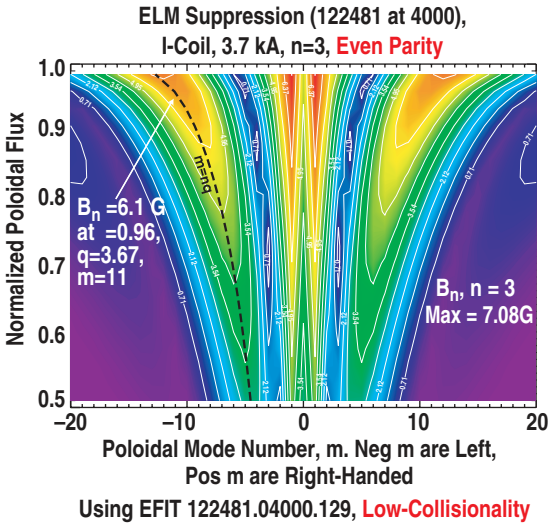

K.H. Burrell Figure 3

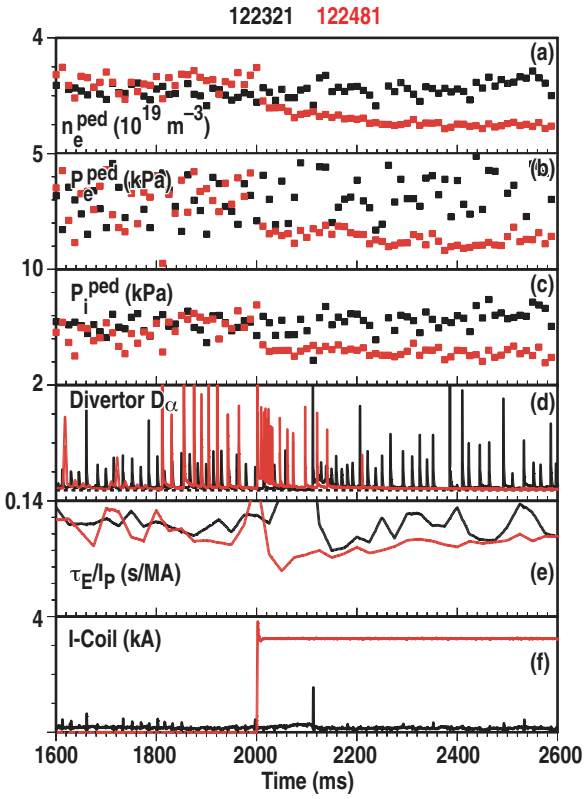

K.H. Burrell Figure 4

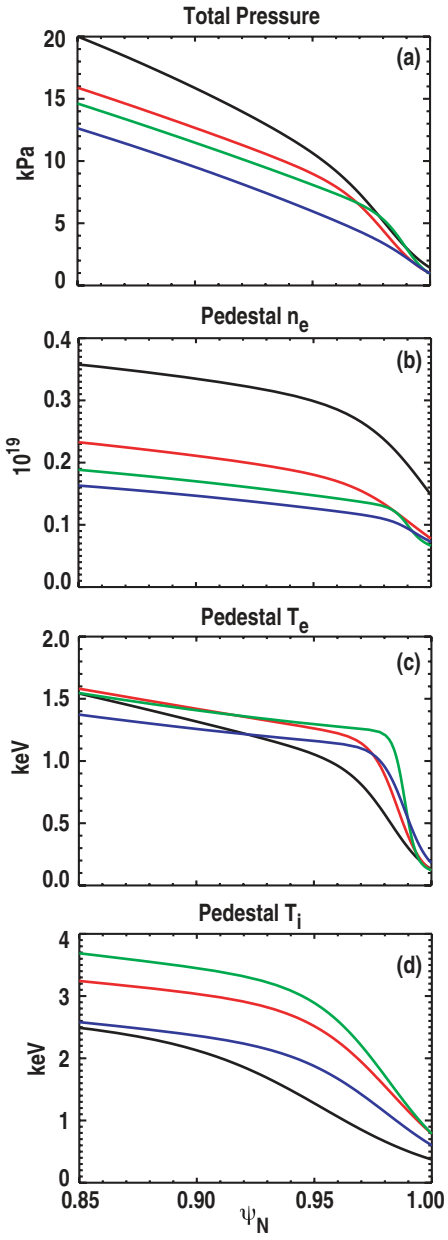

K.H. Burrell Figure 5

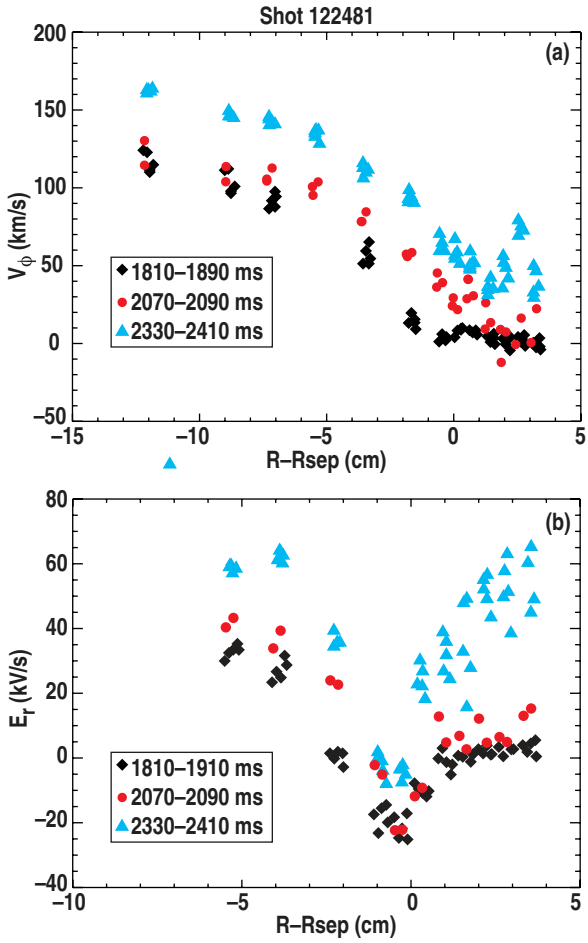

K.H. Burrell Figure 6

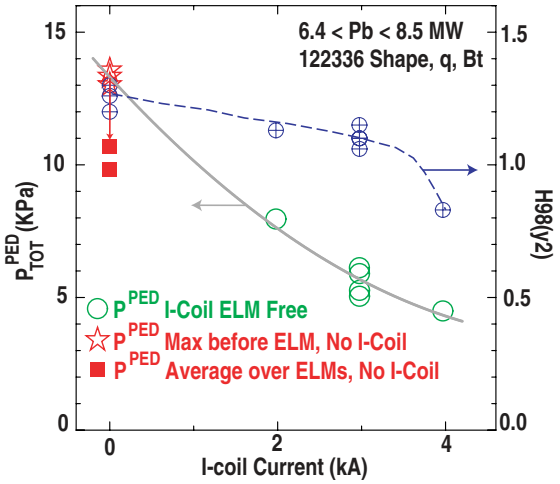

K.H. Burrell Figure 7

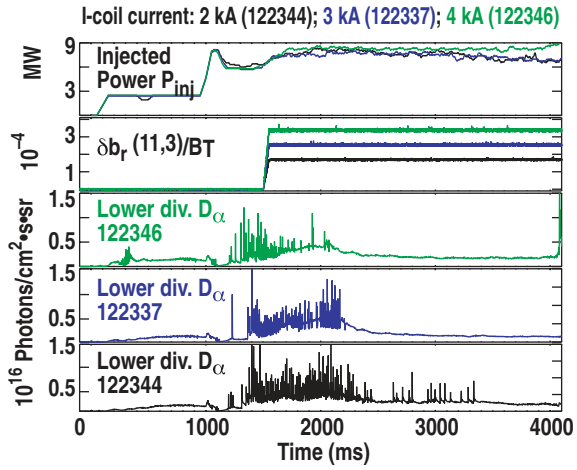

K.H. Burrell Figure 8

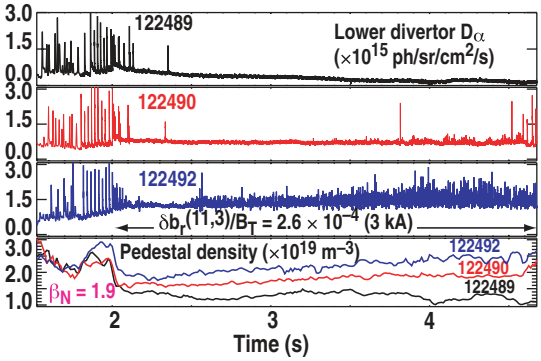

K.H. Burrell Figure 9

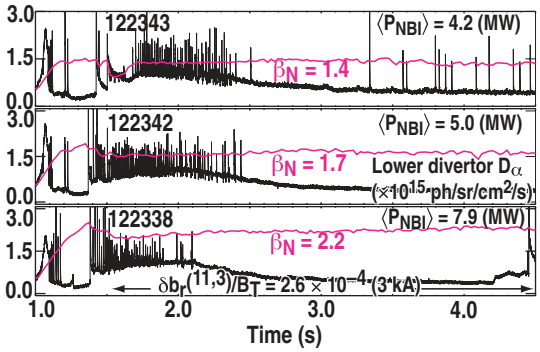

K.H. Burrell Figure 10

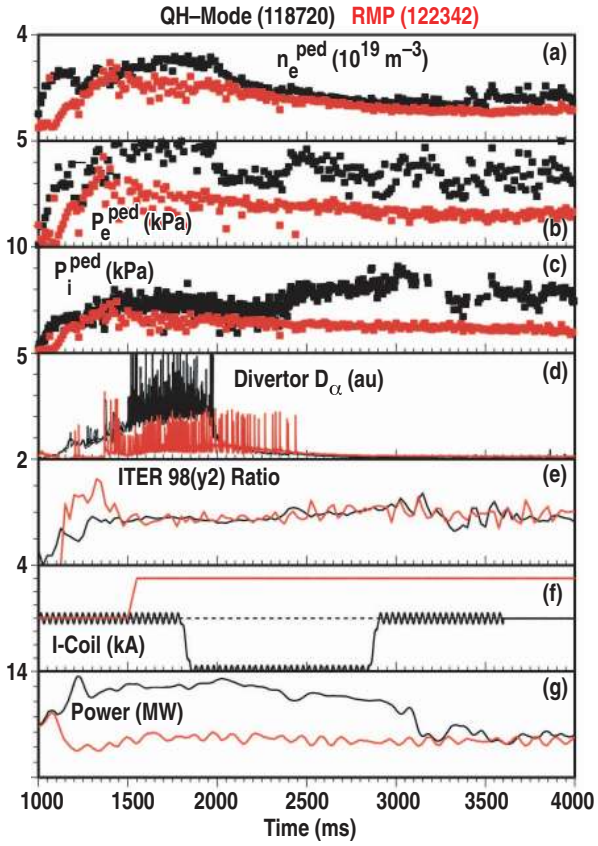

K.H. Burrell Figure 11

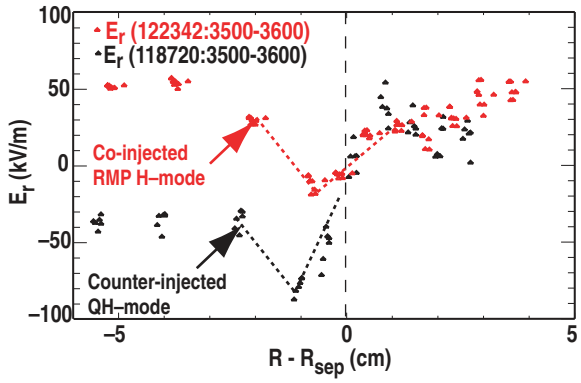

K.H. Burrell Figure 12

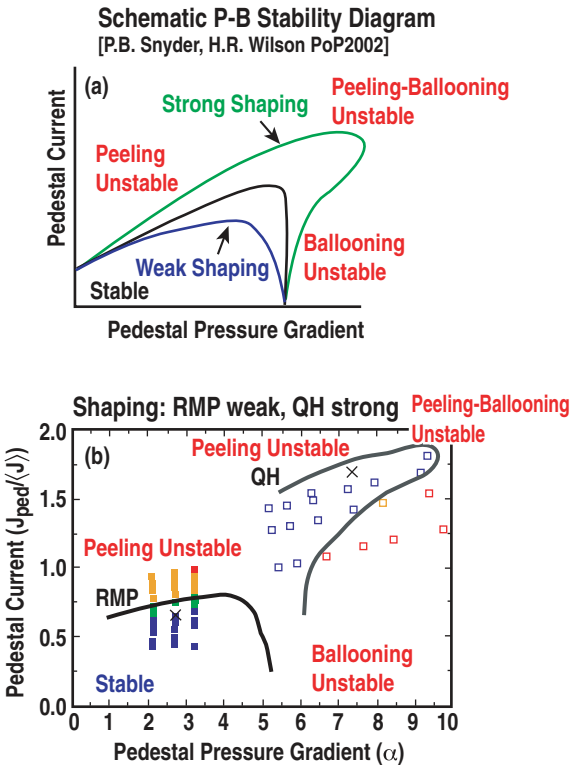

K.H. Burrell Figure 13

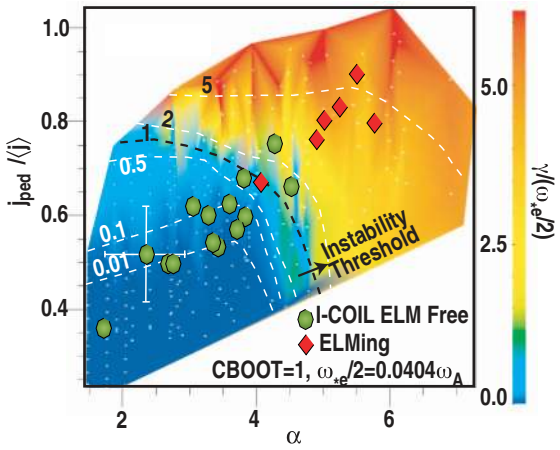

K.H. Burrell Figure 14